Classical analysis of Coulomb effects in strong-field ionization of H_2^+ by intense circularly polarized laser fields

Katharina Doblhoff-Dier,[1,2] Konstantinos I. Dimitriou,[3,4] André Staudte,[5] and Stefanie Gräfe[1,2]

[1]*Institute for Theoretical Physics, Vienna University of Technology, Vienna, Austria*

[2]*Institute for Physical Chemistry, Friedrich-Schiller-University Jena, Jena, Germany*

[3]*Department of Physical Science and Applications, Hellenic Army Academy, Vari, Greece*

[4]*Institute of Theoretical and Chemical Physics, National Hellenic Research Foundation, Athens, Greece*

[5]*Joint Attosecond Science Lab, University of Ottawa and National Research Council of Canada, 100 Sussex Drive Ottawa, Ontario, Canada K1A 0R6*

(Received 23 June 2013; published 10 September 2013)

We analyze the distortion of the molecular frame photoelectron angular distributions of H_2^+ ionized by a strong, circularly polarized infrared laser field using classical trajectory Monte Carlo simulations. We find that the nonisotropic field of the molecular ion rotates the final electron momenta. The degree of distortion from the strong-field approximation's predictions is thereby sensitive to the field strength and the internuclear distance but, counterintuitively, does not necessarily decrease for high field strengths. Furthermore, the distortion also depends crucially on the initial momentum of the classical electron after tunneling, while the exact shape of the ionization rate seems to be less important. A trajectory analysis within our simple model allows us to interpret recent experimental results.

DOI: 10.1103/PhysRevA.88.033411 PACS number(s): 33.60.+q, 33.80.Eh

I. INTRODUCTION

Strong-field–matter interaction is a complex phenomenon, which can be well understood with a few simplifications such as treating the electric field classically and completely neglecting the ionic potential and the electronic structure after ionization. These assumptions form the basis of the strong-field approximation (SFA) [1–3]. Although neglecting the Coulomb potential and the electronic structure of the parent ion after ionization is often a very good approximation, many theoretical and experimental studies have demonstrated clear evidence of the influence of the Coulomb potential on the continuum electron wave packet (e.g., [4–23]). In the strong-field photoelectron spectrum, the influence of the parent ion's potential is responsible for the narrowing of the photoelectron momentum distribution transverse to the field direction (Coulomb focusing) and a distortion of the angular photoelectron distribution (Coulomb asymmetry).

Most of the experimental and theoretical investigations have, however, concentrated their efforts on atomic systems, i.e., on single-center, isotropic Coulomb potentials. Recently, a few experiments have started addressing the role of a nonisotropic Coulomb potential and the electronic structure on molecular photoelectron distributions by studying strong-field ionization of molecules [24–30]. In these experiments, strong deviations of the measured radial and angular photoelectron spectra compared to the predictions from the strong-field approximation were found. Two mechanisms have been invoked to explain the deviations: (a) laser-driven electron dynamics inside the molecule prior to ionization and (b) the long-range Coulomb force. Whereas the bound-electron dynamics can change the timing of ionization and thereby the photoelectron emission angle, the long-range, anisotropic Coulomb field influences the photoelectron momentum for a long time after ionization.

In this work, we present results of classical trajectory Monte Carlo calculations (CTMC) aiming at disentangling the different contributions of (a) the electronic dynamics inside the molecule and (b) the long-range potential leading to a shift of the angular photoelectron distribution. We concentrate on the ionization of the hydrogen molecular ion, H_2^+, at different internuclear distances R and laser intensities I. We distinguish between two different ionization mechanisms, tunnel-type ionization and over-the-barrier ionization, in order to investigate the contributions and the effects of both types. The ionization rate is assumed to follow the Ammosov-Delone-Krainov (ADK) formalism or to mimic the temporal behavior of the rates in the case of multiple-ionization bursts [31,32]. This allows assembling different model systems and comparing their final electron momentum distributions with predictions from the time-dependent Schödinger equation and experiments. Thus, deploying different model systems, we are able to separately describe the influence of the long-range Coulomb part acting on the continuum electron, investigate the strong-field dynamics of the electron, and analyze the influence of the ionization rate.

This paper is organized as follows: after a detailed description of the different model systems used for our classical trajectory calculations in Sec. II, the numerical results are presented in Sec. III. The paper concludes with discussion and summary.

II. MODEL SYSTEMS

Within our CTMC method, classical trajectories describing the electronic dynamics of the hydrogen molecular ion (H_2^+) in the presence of an intense, circularly polarized laser field are propagated in two spatial dimensions, x, y, for fixed internuclear distances R and for an ensemble of initial conditions in coordinate and momentum space right after tunneling. In enhanced ionization of H_2^+, the dissociating molecular ion moves through a range of internuclear separations with an increased ionization probability [33]. When the second

ionization occurs, the molecular ion is projected onto the Coulomb explosion potential, and the dissociation is further accelerated. However, the photoelectron moves about 100 times faster than the protons. In circular polarization, as considered here, the final-state interaction of the photoelectron and parent ion is particularly small and usually negligible [7]. Hence, in our model, we are using the frozen-nuclei approximation; i.e., we neglect the nuclear dynamics after and during the ionization step. This is a widely employed approximation in the calculation of strong-field photoelectron spectra (e.g., [26,34–38]).

The potential of the three-body system is represented by a soft-core potential of the form (atomic units are applied if not stated otherwise)

$$V(x,y) = +\frac{Z^2}{R} - \frac{Z}{\sqrt{(x \pm R/2)^2 + y^2 + a^2}}, \tag{1}$$

where the nuclear charge $Z = 1$ and the soft-core parameter $a = 0.5$. The interaction with the electric field circularly polarized in the molecular plane is

$$W(x,y,t) = xE_x(t) + yE_y(t), \tag{2}$$

and the electric field in the $i = x,y$ direction is

$$E_i(t) = E_0 f(t) \cos(\omega t + \phi_i), \tag{3}$$

where $\phi_i = 0$ and $\pi/2$, respectively, and $\omega = 800$ nm. The field strength E_0 is varied to give intensities between 6×10^{13} and 1.5×10^{15} W/cm^2. The pulse envelope $f(t)$ is given by a 50-fs full width at half maximum $\sin^2$ pulse. The trajectories are propagated solving Newton's equation in two dimensions using a standard second-order Runge-Kutta algorithm, with the total potential consisting of the sum of Eqs. (1) and (2). Neglecting the potential part described in Eq. (1), the trajectories are only subject to the laser field. This represents the classical analogon to the strong-field approximation (CSFA). Typically, 100 000 trajectories are propagated. The ionization time is restricted to the central field cycle.

For the laser parameters used, the Keldysh parameter $\gamma = \omega\frac{\sqrt{2I_P}}{E_0} \sim 1$. This clearly represents an intermediate regime between multiphoton ionization and tunnel ionization. Often, the tunneling picture is invoked in the interpretation of results even in this intermediate regime. In our study, we apply tunneling conditions for both the initial coordinate and momentum values of the trajectories and the ionization rate (following the Delone-Krainov expression [39]). These conditions are then slightly modified, allowing us to investigate to what extent the experimental results can be described within the simple tunnel picture by comparing our simulations with experimental results. The exact initial conditions for the electron trajectories are specified in what follows.

A. Initial distribution in momentum space

In the case of tunnel ionization, the initial momentum distribution at the time of ionization is assumed to follow the Delone-Krainov momentum distribution [39]. When ionization proceeds via over-the-barrier ionization (OBI), a Gaussian-shaped isotropic momentum distribution in the x,y direction is assumed, where the width of the distribution is fitted to a quantum-mechanical (field-free) ground-state wave function, thus mimicking a microcanonical ensemble. Typically, OBI of atoms is described with initial conditions corresponding to a microcanonical ensemble [40,41]. Such a description may cause inaccuracies, as the electron distribution in a molecule subject to a strong electric field is strongly distorted by the field.

It is still under discussion whether in the case of OBI, upon ionization, the electron trajectories will have an average momentum different from zero. This is why we have also tested the assumption that the initial electron momentum distribution is centered around nonzero momentum values,

$$\vec{p}_0 = \sqrt{2(-I_P - V_{\max})}, \tag{4}$$

where I_P is the ionization potential (see Sec. II C) and $V_{\max}$ is the maximum height of the barrier.

B. Initial distribution in coordinate space

Within the tunneling regime, for atoms, the starting condition in coordinate space is typically expressed as $r_0 = (x_0, y_0) = (-I_P/E(t_0),0)$ for fields linearly polarized in the x direction. For molecules, we have to consider that neither the potential nor the ionization rate is isotropic. Thus, we numerically search for the tunnel exit, which is found when the following conditions are met:

$$\frac{\vec{r}_0}{|r_0|} = -\frac{\vec{E}}{|E|}, \quad V\left(-\frac{|r_0|}{|E|} \cdot \vec{E}\right) = I_P. \tag{5}$$

We mimic the fact that ionization of H_2^+ is preferred along the internuclear axis by replacing the electric field entering the ADK rate by the x component of the field E_x only. In the case of OBI, the initial conditions in coordinate space are defined to be on top of the barrier, $V_{\max}$.

Tunneling ionization is used if $(-I_P)$ is lower in energy than $V_{\max}$. If $(-I_P)$ is higher in energy than $V_{\max}$, then OBI is simulated. The ionization potential I_P itself is model dependent and is specified in the following section.

C. Ionization potential: Floquet vs field-dressed states

For the ionization potential, we have compared three different models: First, we used a field-free ionization potential $I_P(R) = Z^2/R - V_i(R)$ $(i = g,u)$, where Z^2/R is the repulsive potential of H_2^{2+} and $V_g(R)$ and $V_u(R)$ are the two lowest-lying Born-Oppenheimer potentials of H_2^+. Second, we employed a light-induced ionization potential where $I_P(R) = Z^2/R - V_i(R)$, with $V_i^{LI}(R), i = \text{low, up}$, are the light-induced (LI) states obtained for each value of the internuclear distance R via the unitary transformation

$$U \begin{pmatrix} V_g & -\mu E_x \\ -\mu E_x & V_u \end{pmatrix} U^\dagger = \begin{pmatrix} V_{\text{low}}^{LI} & 0 \\ 0 & V_{\text{up}}^{LI} \end{pmatrix}. \tag{6}$$

Finally, we applied an ionization potential defined by the difference potential of H_2^{2+} with the Floquet eigenenergies

$$\begin{aligned} V_{\text{low}}^{\text{Floquet}} &= -(V_u - V_g)/(2\omega)\, J_0(\zeta) + 0.5(V_u + V_g), \\ V_{\text{up}}^{\text{Floquet}} &= +(V_u - V_g)/(2\omega)\, J_0(\zeta) + 0.5(V_u + V_g), \end{aligned} \tag{7}$$

where $J_0(\zeta)$ are the Bessel functions and $\zeta = 2\mu E_0/\omega$ [32].

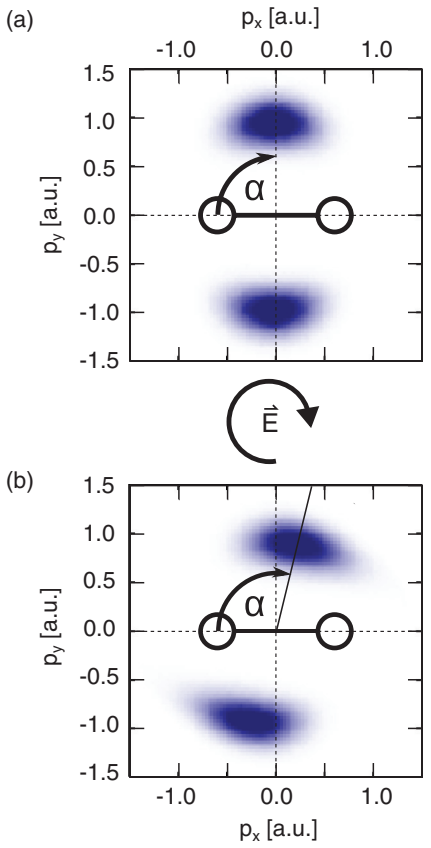

FIG. 1. (Color online) Final momentum distribution of electrons (a) neglecting the Coulomb potential after ionization and (b) including the Coulomb potential for the continuum electrons. Internuclear distance $R = 2$ Å, laser intensity is 1.5×10^{14} W/cm^2, and laser rotation is clockwise. The molecule here and in what follows is aligned along the x axis.

If not specified otherwise, the light-induced potentials Eq. (6) were used. When calculating the ionization rates according to the Delone-Krainov equation, the ionization potential was additionally shifted by

$$\tilde{I}_p = I_p \pm E_x \frac{R}{2} \tag{8}$$

for the lower and upper wells, respectively, in order to account for the spatial extension of the molecule.

III. NUMERICAL RESULTS

In our numerical simulations, we apply a 50-fs ($\sin^2$, full width at half maximum) circularly polarized laser field with a central wavelength of 800 nm. The intensity and the internuclear distance are varied. Ionization is restricted to the central cycle of the field.

In the absence of any molecular potential after ionization, a classical variant of the strong-field approximation is recovered (see Sec. II): the electron in the continuum is only subject to the circularly polarized laser field, and the final momentum distribution of the electrons [Fig. 1(a)] is centered around $p_x = 0, p_y \approx \pm 0.9$ a.u. (for a field strength of $E_0 = 0.055$ a.u.). This is in correspondence with the strong-field approximation, where the final momentum value is defined by the vector potential of the electrons at the moment (t_b) of birth, $\vec{p}_f = -\vec{A}(t_b)$. Since ionization is preferred along the internuclear axis (x axis), ionization occurs predominantly at times when E_x is large. At these times, the vector potential A_y is large, and electrons in the continuum are rotated into the y direction.

In the presence of the molecular potential, the momentum distribution is rotated, such that the maximum of the distribution is not centered around $p_x = 0$ but around a nonzero value p_x, as displayed in Fig. 1(b). The degree of rotation has been related to the strength of the parent ion's influence on the leaving electron [26]. In order to allow for a quantitative description, we define the mean angle α as the weighted mean of the rotation angle's probability distribution. Taking the sense of rotation of the circularly polarized field and the result expected from SFA into account, we further define 0° to correspond to $p_x < 0$, $p_y = 0$ and 90° to correspond to $p_y > 0$, $p_x = 0$ (see Fig. 1). Since the probability distribution is π periodic, the mean is calculated from the minimum of the probability distribution in the first or fourth quadrant to the minimum in the second or third quadrant. An angle $\alpha = 90^\circ$ thus corresponds to the SFA result, and the angle increases in the direction of the circularly polarized light.

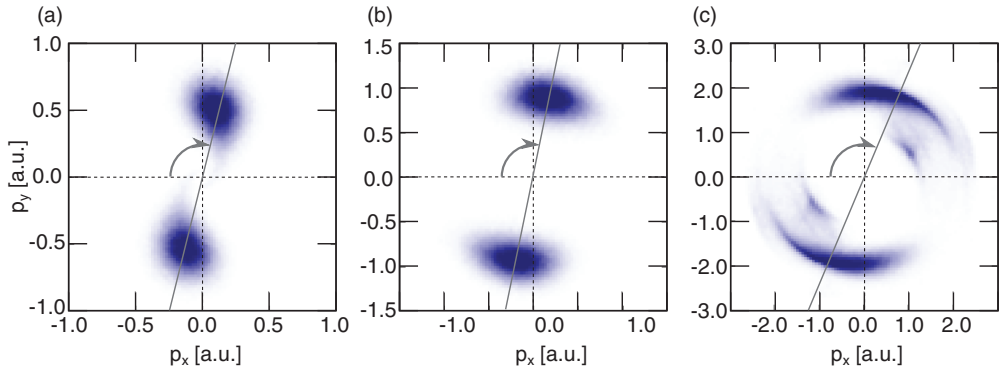

FIG. 2. (Color online) Electron momentum distribution with Coulomb potential for $R = 1.5$ Å while varying the laser intensity: (a) $I_a = 6 \times 10^{13}$ W/cm^2, (b) $I_b = 1.5 \times 10^{14}$ W/cm^2, and (c) $I_c = 6 \times 10^{14}$ W/cm^2. Note the different axis ranges.

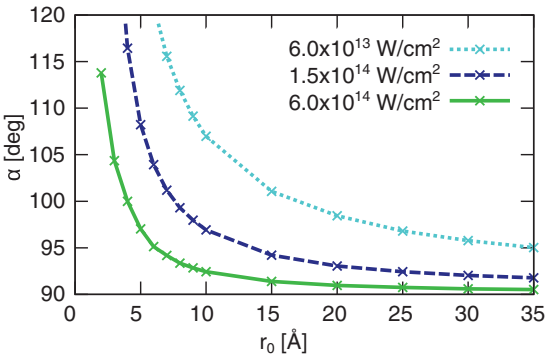

FIG. 3. (Color online) Rotation angle α as extracted from the final momentum distribution of electrons as a function of the starting value $r_0 = (x_0, y_0)$, with $x_0 = -r_0 \cos\varphi - R/2 \cos\varphi, y_0 = -r_0 \sin\varphi$, where $\tan\varphi = E_x/E_y$. The internuclear distance R is fixed at $R = 3$ Å.

In what follows, we analyze the dependence of the mean rotation value α on the internuclear distance and the laser intensity.

A. Dependence of the Coulomb-field-induced rotation on the intensity and internuclear distance

First, we explore the influence of the laser intensity on the mean rotation angle α for a fixed internuclear distance R. As can be gathered from Fig. 2, we find that the value of the rotation angle α shifts away from 90° for increasing field strengths. In other words, the larger the laser field strength is, the larger the distortion by the Coulomb potential is. At first sight, this is surprising since one would expect the influence of the Coulomb potential to decrease compared to the influence of the electric field for higher intensities. However, the result can be understood by the fact that, for larger field strengths, the tunnel exit r_0 of the electron [with r_0 approximately given by $-I_p/E(t_0)$] is closer to the nucleus, leading to a larger distortion of the electron upon entering the continuum. In order to underline this statement, we present in Fig. 3 the dependence of the rotation angle α on the initial coordinate r_0 (the tunnel exit) of the electron in coordinate space: instead of finding the tunnel exit according to Eq. (5), we varied r_0 for a fixed internuclear distance $R = 3$ Å and for three different laser intensities, $I_1 = 6.0 \times 10^{13}$ W/cm^2, $I_2 = 1.5 \times 10^{14}$ W/cm^2, and $I_3 = 6.0 \times 10^{14}$ W/cm^2. Now, the intuitive picture is recovered where the higher the intensity and the larger the distance of the initial coordinate r_0 from the parent ion are, the smaller the Coulomb-induced shift on the electron is and the lower the deviation of α away from 90° is.

Next, we examine the dependence of the mean rotation angle α on the internuclear distance. Figure 4 demonstrates that the rotation angle α increases for increasing internuclear distances as long as ionization proceeds below the barrier. The reason for the strong internuclear distance dependence is that the ionization potential I_P is lowered as a function of internuclear distance: the larger R is, the smaller I_P is, and in turn, the closer the tunnel exit $r_0 \approx -I_P/E(t_0)$ is to the nucleus, and thus, the stronger the distortion by the Coulomb potential on the outgoing electron is.

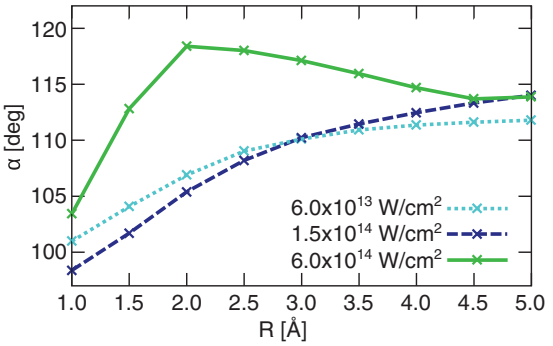

FIG. 4. (Color online) Rotation angle α as extracted from the final momentum distribution of electrons as a function of the internuclear distance R. The general trend is that the rotation angle increases for increasing internuclear distances. The elbow in the curve for $I = 6.0 \times 10^{14}$ W/cm^2 is due to the transition to over the barrier ionization.

So far, we have focused on the mean rotation angle α integrated over the final radial momenta of the electrons. However, previously, it was shown that the mean rotation angle can depend strongly not only on the final electron energy but also on the internuclear separation [26,29]. In Fig. 5,

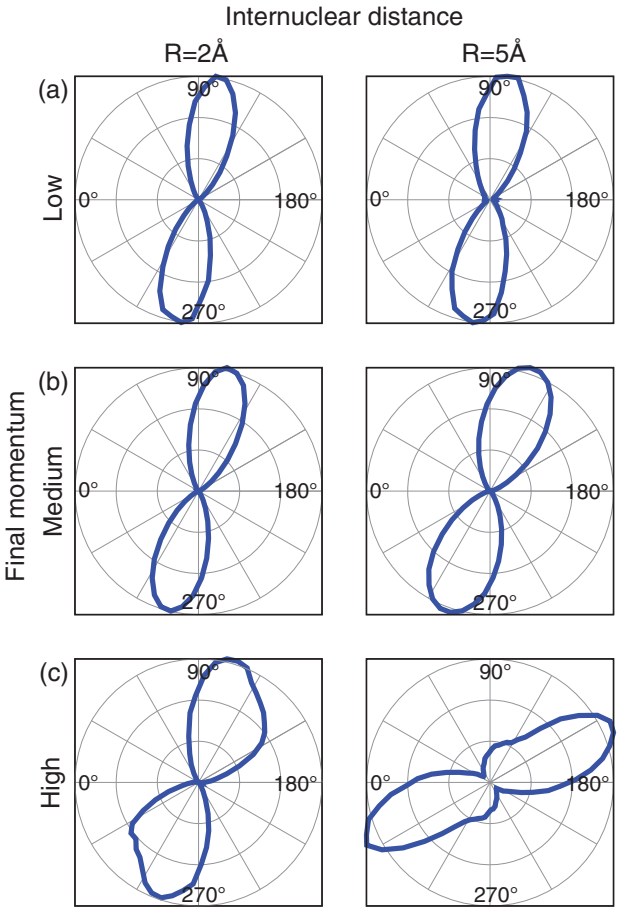

FIG. 5. (Color online) Polar representation of the angular distribution of electrons resolved by the final momentum p_f (see text): (a) $p_f < 0.7$ a.u., (b) $0.7 \leqslant p_f \leqslant 1.2$ a.u., and (c) $1.2 > p_f$ a.u., shown for two different internuclear distances, $R = 2$ Å and $R = 5$ Å. The Laser intensity is $I = 1.5 \times 10^{14}$ W/cm^2.

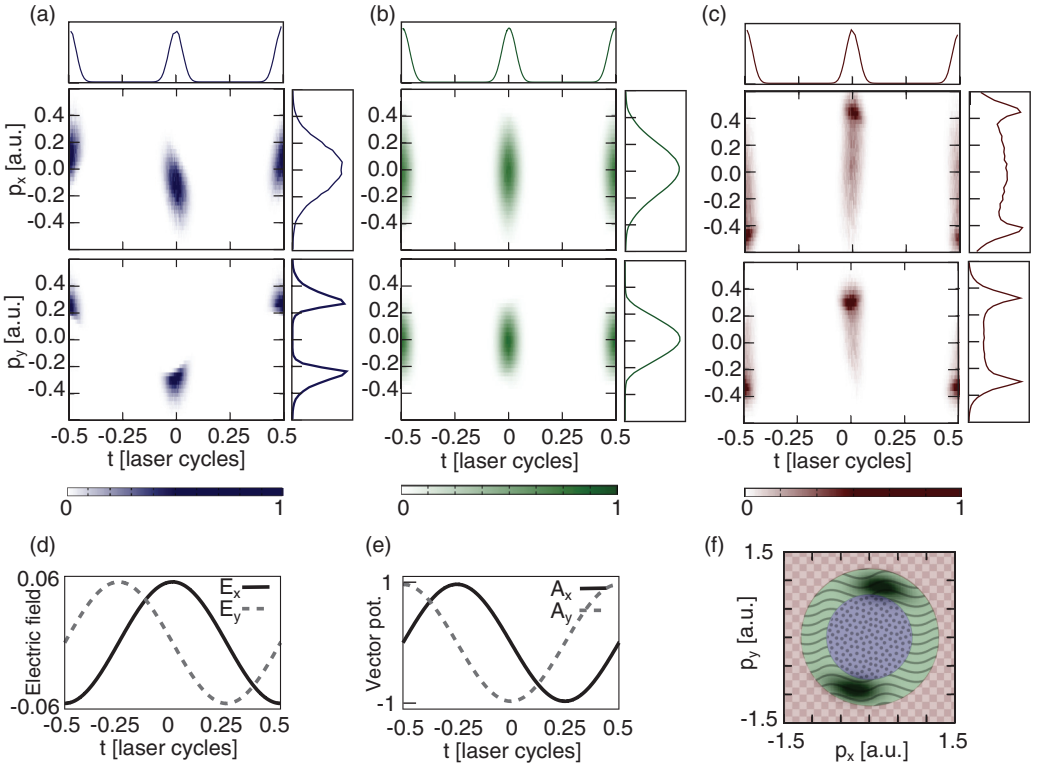

FIG. 6. (Color online) (f) Mapping from the final momentum distributions to the initial conditions (momentum in the x and y directions resolved for the time of birth t_b and the two-dimensional projections thereof) for (a) slow electrons with $p_f < 0.7$ a.u. ($E_f^{\rm kin} < 6.7$ eV), marked by the dotted blue region in (f), (b) medium electrons with $0.7 \leqslant p_f \leqslant 1.2$ a.u. (6.7 eV$\leqslant E_f^{\rm kin} \leqslant$ 19.6 eV), marked by the green region with waves in (f), and (c) fast electrons with $p_f > 1.2$ a.u. (19.6 eV$> E_f^{\rm kin}$), marked with the red squares in (f). (d) The electric field $\vec{E}$ and (e) the vector potential A.

the angle distribution of the final momenta, integrated over different final electron energies, is shown in polar coordinates for two different internuclear separations. In order to ease the comparison with the experiment [29], we choose three radial momentum ranges (rows) and two internuclear separations (columns). At an internuclear separation of 2 Å (left column), electrons with low final momentum $p_f < 0.7$ a.u. ($p_f^2 = p_x^2 + p_y^2$), corresponding to an energy of $E_f^{\rm kin} < 6.7$ eV, are preferentially emitted at angles $\alpha \approx 100^\circ$ [Fig. 5(a)]. Electrons with a final momentum $0.7 \leqslant p_f \leqslant 1.2$ a.u. (6.7 eV $\leqslant E_f^{\rm kin} \leqslant$ 19.6 eV) are emitted over a wider range of angles peaking at $\alpha = 105^\circ$ [Fig. 5(b)]. Finally, electrons with the highest momentum $p_f > 1.2$ a.u. (19.6 eV $> E_f^{\rm kin}$) are preferentially emitted to even larger angles around $\alpha = 120^\circ$ [Fig. 5(c)]. In good qualitative agreement with the experiment and the time-dependent Schrödinger equation calculations [29], our model shows that larger final radial momenta experience a stronger distortion. For a larger internuclear separation (right column of Fig. 5) the rotation in our simulation is generally larger, thereby also reproducing the trend observed in the experiment.

Having established the agreement between our simulation and the experimental results, we will now take advantage of the fact that our investigations are based on classical calculations, which allows us to interpret and analyze the results in terms of trajectories. By virtue of a one-to-one mapping in configuration space, we can follow the electrons with low, medium, and high final momenta backwards in time and associate the initial conditions, i.e., the time of birth t_b, the birthplace $\vec{r}_0$, and the initial momenta $\vec{p}_0$, of the respective trajectories. Such a mapping is presented in Fig. 6.

While the probability distributions of the time of birth t_b of all trajectories are all peaked around the maximum of the electric field in the x direction E_x [see top panels of Figs. 6(a), 6(b), and 6(c)] without any significant time shift, the initial momentum distributions differ significantly for different final momenta [see lower color map images in Figs. 6(a), 6(b), and 6(c)]. Fast trajectories [Fig. 6(c)] are born with a large initial y momentum p_y^0 opposing the direction of the instantaneous y-vector potential A_y [cf. Fig. 6(e)]. For fast trajectories, the initial momentum p_y^0 in the y direction thus adds to the final momentum expected from SFA $\vec{p}_f^{\,SFA} = -\vec{A}(t_B)$, leading to a high final momentum p_f. The opposite is true for the slow trajectories [cf. Fig. 6(a)]. The role of the initial transversal momentum p_y^0 is thus primarily to define the final momentum p_f.

Additionally, the initial momentum in the x direction differs for the slow and fast trajectories: For fast trajectories, the initial x momentum is large and points in the direction of the electric field at the time of birth $E_x(t_b)$, while for slow electrons, it opposes the x electric field. Since the tunnel exit lies in the $(-E_x)$ direction, the fast trajectories start off with a momentum component pointing backwards, in the direction of the nucleus, whereas the slow trajectories directly head

away from the nucleus while being decelerated by the nuclear attraction. Consequently, the fast trajectories come very close to the nuclei, feel a very strong Coulombic force, and are hence rotated strongly.

Within the model used, the initial momentum distribution in the x direction p_x^0, i.e., parallel to the electric field at the time of birth, plays a major role since it seems to be responsible for the experimentally observed strong rotation of the fast trajectories. If the momentum distribution parallel to the electric fields were neglected and p_x^0 were set to zero, the experimental finding would not be reproduced. Therefore, this model suggests that the often neglected momentum distribution parallel to the field may play an essential role.

We note parenthetically that the initial x momentum is not the only possible way to reproduce the experimental results. One possibility is to restrict the starting point of the trajectories to the x axis. This modifies the time of birth distributions: Slow trajectories are then born before the maximum of E_x, while fast trajectories are still born mainly at the maximum of E_x, which would also lead to a stronger rotation of fast trajectories. Based on highly accurate calculations and experimentally accessible data of the angle-dependent ionization probability [24,26,42], we believe, however, that this quasi-one-dimensional picture is less likely to describe the physical process than our approach in which the tunnel exit is not clamped to the molecular axis.

So far we have assumed that the tunneling picture holds and that ionization occurs from the lower field-dressed state [Eq. (6)] via tunneling. For the major part of the results presented in the last section, neither OBI nor any electronic dynamics prior to ionization was included. (The only exception is Fig. 4, where OBI was included at high intensities and large internuclear distances: $I = 6.0 \times 10^{14}$ W/cm^2 for $R \geqslant 2.0$ Å.) Now, we address the possibility of OBI occurring at lower intensities as well as electronic dynamics by mimicking different ionization rates.

B. Towards a description of OBI in molecules

First, we aim at including the contribution of ionization from the upper field-dressed state. Ionization from the upper field-dressed state is, for the values of R used, in almost all cases above the internuclear barrier. As described in Sec. II, we mimic OBI by choosing an isotropic initial momentum distribution with a (Gaussian) width of 0.44 a.u. Including OBI, which originates from an estimated amount of 10% of the population in the upper field-dressed state (estimated from the time-dependent Schrödinger equation calculations), does not change the result for the momentum-integrated angle α much (figure not shown).

Note that our model approximating OBI via isotropically distributed initial momenta starting on top of the internuclear barrier is sensitive to changes in the initial conditions. Changing the initial coordinate such that the trajectories start near one nucleus changes the rotation angle substantially. Thus, the results obtained within our OBI model should be taken with care.

C. Non-ADK-type ionization in the over-the-barrier regime

The ionization rate of a molecule is typically described by (molecular) ADK. In Ref. [26] it was suggested that

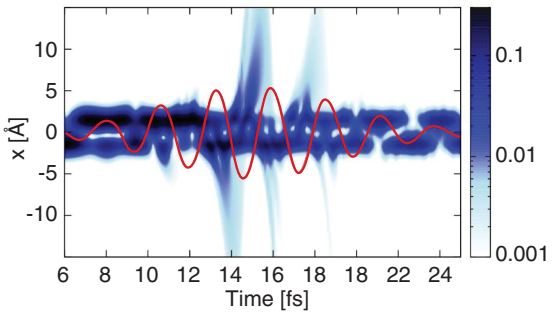

FIG. 7. (Color online) Electronic density $\rho(x,t) = \int \mathrm{d}y\, |\psi(x,y,t)|^2$ obtained from a two-dimensional calculation of the time-dependent Schrödinger equation with nuclei fixed at 3 Å subject to a short, 10-fs (Gaussian FWHM), circularly polarized laser field.

electron localization dynamics in the hydrogen molecular ion in the enhanced ionization region result in multiple ionization bursts (MIB), which were made primarily responsible for the deviations of the rotation angle α from 90°.

For visualization, we numerically integrated the time-dependent Schrödinger equation on a grid in two spatial dimensions using the same Hamiltonian as for the classical model (i.e., including the soft-core potential, using circularly polarized light in dipole approximation). The internuclear distance is set to $R = 3$ Å, and for computational reasons, the pulse length is reduced to 10 fs (Gaussian FWHM). Figure 7 displays the time evolution of the electronic density $\rho(x,t) = \int \mathrm{d}y |\psi(x,y,t)|^2$ obtained from the solution of the time-dependent Schrödinger equation. The multiple ionization bursts per laser half cycle (as in Refs. [31,32]) are clearly visible, e.g., near $t = 13$,14.5, and 16 fs. Further, it can be seen that the electron localizes near the left or right potential well. At this internuclear distance, $R = 3$ Å, ionization does not follow the ADK rate at all, and bound electron dynamics prior to ionization plays a major role.

In the following, we include an ionization rate mimicking a multi-ionization burst structure, which has been related to electron localization dynamics in Floquet states [31]. We hence use Eq. (7) to determine the electron localization as in Ref. [31]. The ionization rate is then assumed to be given by

$$\Gamma_{l/r}^{\mathrm{MIB}} = \Gamma^{\mathrm{ADK}} e^{-\alpha(p_{l/r}-0.5)}, \tag{9}$$

where Γ^{ADK} is the Delone-Krainov ionization rate used before, $\alpha = 50$ is a parameter controlling the modulation depth of the multiple ionizations, and $p_{l/r}$ is the probability of finding the electron at the left and right nucleus, respectively. Despite the strong non-ADK-like ionization, the precise form of the ionization rate seems to be of minor importance. For the tested OBI models, changing the ionization rate to multiburst structure induced only minor changes to the average shift [cf. Figs. 8(a) and 8(b)]. The change of I_P due to switching from Eq. (6) to Eq. (7), however, introduced noticeable changes. However, none of the models induce a shift different from 90° if the Coulomb continuum after ionization is switched off [Fig. 8(c)], demonstrating thus the importance of the long-range Coulomb potential. In other words, independent

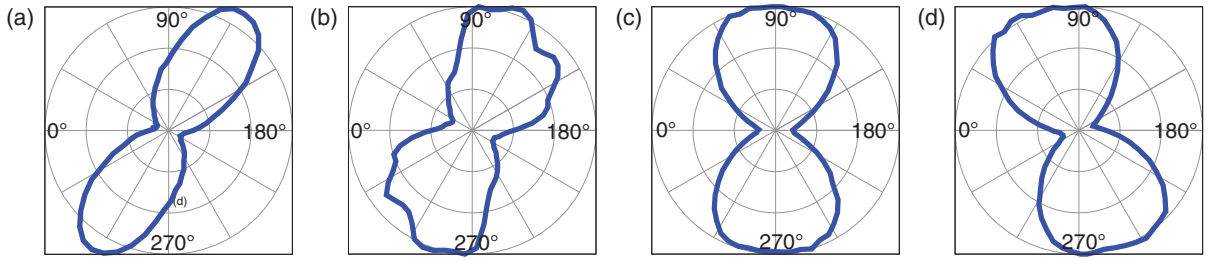

FIG. 8. (Color online) Polar representation of the angular distribution of electrons for the final momentum range $0.7 \leqslant p_f \leqslant 1.2$ a.u. (see text): (a) using the ADK rate and I_P defined for the lower Floquet state [Eq. (7)], (b) assuming multi-ionization bursts, (c) assuming multi-ionization bursts, but neglecting the Coulomb continuum, and (d) assuming multi-ionization bursts, neglecting the Coulomb continuum, together with an initial momentum p_0 as defined in Eq. (4). Calculations are for $R = 3$ Å, laser intensity $I = 1.5 \times 10^{14}$ W/cm^2.

of whether electronic ionization is below the barrier or over the barrier or whether multiple ionization bursts are present, without a Coulomb continuum, an SFA-type momentum distribution is recovered.

In Ref. [29], it was demonstrated with the help of a quantum model capturing the bound-state dynamics but coupling it to a flat continuum (i.e., without Coulomb effects) that the combination of the multiburst ionization rate, the bound-state electronic dynamics, and, in particular, a significant initial momentum upon ionization may lead to a rotated momentum distribution. However, it was also shown that the model neglecting the Coulomb influence in the continuum cannot reproduce the direction of the rotation correctly. This seems to hold also for our CTMC calculations: Including an initial momentum according to Eq. (4) but neglecting the Coulomb potential in the continuum, a rotation of the momentum distribution is observed, but in the direction opposite to the shift of the Coulomb field, resulting in $\alpha < 90^\circ$ [see Fig. 8(d)]. Possibly, these OBI events correspond to the experimentally observed "lobes" of the momentum distribution related to electrons rotated into directions significantly different from the main rotation direction.

We would like to stress that our CTMC calculation cannot exclude delayed emission, which was found in other calculations using a fermion molecular dynamics model as the dominant mechanism [43]. However, our model strongly suggests that to reproduce the experimentally measured shift of the momentum distribution, inclusion of the molecular Coulomb continuum is necessary.

IV. DISCUSSION AND SUMMARY

We have presented results of classical trajectory Monte Carlo calculations simulating the ionization of H_2^+ in intense, circularly polarized laser fields. Our simulations aim at examining to what extent the experimental results can be described within the tunneling picture and at investigating the influence of the nonisotropic Coulomb potential on the photoelectron momentum distribution. This is achieved by comparing the angular distribution of the electron momentum spectra at different laser intensities and internuclear distances while varying the initial conditions of the electron trajectories and the ionization rate. In our simulation, we can neglect the Coulomb field in the propagation of the electron trajectories and are thus able to extract the influence of the Coulomb continuum.

Our model provides an explanation for the counterintuitive fact that the deviation from the SFA predictions does not necessarily decrease at higher field strengths: the tunnel exit moves closer to the Coulombic center at higher field strengths, leading to a stronger distortion of the trajectories at the initial stage after tunneling. Furthermore, we indicate the importance of the initial momentum distribution of the classical electrons in interpreting momentum-resolved angular distributions of the final momentum by mapping the initial conditions of the trajectories to final momenta and comparing with experimental results [29]. Investigating the influence of the precise form of the ionization rate, we show that the shift of the rotation is largely insensitive to whether the ionization rate follows a Delone-Krainov form or features a multiburst structure. In contrast, the inclusion of the Coulomb field is a requisite to obtain a non-SFA-like momentum distribution, as has been observed experimentally [29]. Allowing for a nonzero initial momentum in combination with the multiburst ionization rate, as done in Ref. [26], leads to a shift of the mean rotation angle towards smaller values. Our results encourage further investigations of classical electron dynamics in nonisotropic Coulomb fields possibly extending to a classical description of enhanced ionization and over-the-barrier dynamics.

ACKNOWLEDGMENTS

K.D.D. acknowledges funding from the International Max-Planck Research School for Advanced Photon Science (IMPRS-APS). S.G. gratefully acknowledges financial support from the Austrian Science Fund FWF, Project No. V193-N16.

[1] L. Keldysh, Zh. Eksp. Teor. Fiz. **47**, 1945 (1964)[Sov. Phys. JETP **6**, 1307 (1965)].
[2] F. H. M. Faisal, J. Phys. B **6**, L89 (1973).
[3] H. R. Reiss, Phys. Rev. A **22**, 1786 (1980).
[4] M. Abu-samha, D. Dimitrovski, and L. B. Madsen, J. Phys. B **41**, 245601 (2008).
[5] T. Brabec, M. Y. Ivanov, and P. B. Corkum, Phys. Rev. A **54**, R2551 (1996).

[6] A. Rudenko, K. Zrost, T. Ergler, A. B. Voitkiv, B. Najjari, V. L. B. de Jesus, B. Feuerstein, C. D. Schröter, R. Moshammer, and J. Ullrich, J. Phys. B **38**, L191 (2005).
[7] D. Comtois, D. Zeidler, H. Pépin, J. C. Kieffer, D. M. Villeneuve, and P. B. Colkum, J. Phys. B **38**, 1923 (2005).
[8] X. Xie, S. Roither, D. V. Kartashov, E. Persson, D. G. Arbó, L. Zhang, S. Gräfe, M. Schöffler, J. Burgdöfer, A. Baltuška *et al.*, Phys. Rev. Lett. **108**, 193004 (2012).
[9] M. Bashkansky, P. H. Bucksbaum, and D. W. Schumacher, Phys. Rev. Lett. **60**, 2458 (1988).
[10] G. G. Paulus, F. Grasbon, A. Dreischuh, H. Walther, R. Kopold, and W. Becker, Phys. Rev. Lett. **84**, 3791 (2000).
[11] S. P. Goreslavski, G. G. Paulus, S. V. Popruzhenko, and N. I. Shvetsov-Shilovski, Phys. Rev. Lett. **93**, 233002 (2004).
[12] K. I. Dimitriou, D. G. Arbó, S. Yoshida, E. Persson, and J. Burgdörfer, Phys. Rev. A **70**, 061401(R) (2004).
[13] C. I. Blaga, F. Catoire, P. Colosimo, G. G. Paulus, H. G. Muller, P. Agostini, and L. F. DiMauro, Nat. Phys. **5**, 335 (2009).
[14] W. Quan, Z. Lin, M. Wu, H. Kang, H. Liu, X. Liu, J. Chen, J. Liu, X. T. He, S. G. Chen *et al.*, Phys. Rev. Lett. **103**, 093001 (2009).
[15] C. Liu and K. Z. Hatsagortsyan, Phys. Rev. Lett. **105**, 113003 (2010).
[16] S. Gräfe, J. Doose, and J. Burgdörfer, J. Phys. B **45**, 055002 (2012).
[17] A. Kästner, U. Saalmann, and J.-M. Rost, Phys. Rev. Lett. **108**, 033201 (2012).
[18] C. Lemell, K. I. Dimitriou, X.-M. Tong, S. Nagele, D. V. Kartashov, J. Burgdörfer, and S. Gräfe, Phys. Rev. A **85**, 011403(R) (2012).
[19] C. Lemell, J. Burgdörfer, S. Gräfe, K. I. Dimitriou, D. G. Arbó, and X.-M. Tong, Phys. Rev. A **87**, 013421 (2013).
[20] C. Vozzi, M. Negro, F. Calegari, G. Sansone, M. Nisoli, S. D. Silvestri, and S. Stagira, Nat. Phys. **7**, 822 (2011).
[21] D. Shafir, B. Fabre, J. Higuet, H. Soifer, M. Dagan, D. Descamps, E. Mével, S. Petit, H. J. Wörner, B. Pons *et al.*, Phys. Rev. Lett. **108**, 203001 (2012).
[22] P. Eckle, A. N. Pfeiffer, C. Cirelli, A. Staudte, R. Dörner, H. G. Muller, M. Büttiker, and U. Keller, Science **322**, 1525 (2008).
[23] A. N. Pfeiffer, C. Cirelli, M. Smolarski, D. Dimitrovski, M. Abu-samha, L. B. Madsen, and U. Keller, Nat. Phys. **8**, 76 (2012).
[24] A. Staudte, S. Patchkovskii, D. Pavičić, H. Akagi, O. Smirnova, D. Zeidler, M. Meckel, D. M. Villeneuve, R. Dörner, M. Y. Ivanov *et al.*, Phys. Rev. Lett. **102**, 033004 (2009).
[25] M. Busuladžić, A. Gazibegović-Busuladžić, and D. B. Milošević, Phys. Rev. A **80**, 013420 (2009).
[26] M. Odenweller, N. Takemoto, A. Vredenborg, K. Cole, K. Pahl, J. Titze, L. P. H. Schmidt, T. Jahnke, R. Dörner, and A. Becker, Phys. Rev. Lett. **107**, 143004 (2011).
[27] K. J. Yuan and A. D. Bandrauk, Phys. Rev. A **84**, 013426 (2011).
[28] J. Wu, M. Meckel, S. Voss, H. Sann, M. Kunitski, L. P. H. Schmidt, A. Czasch, H. Kim, T. Jahnke, and R. Dörner, Phys. Rev. Lett. **108**, 043002 (2012).
[29] M. Spanner, S. Gräfe, S. Chelkowski, D. Pavičić, M. Meckel, D. Zeidler, A. B. Bardon, B. Ulrich, A. D. Bandrauk, D. M. Villeneuve *et al.*, J. Phys. B **45**, 194011 (2012).
[30] K. J. Yuan and A. D. Bandrauk, J. Phys. B **45**, 105301 (2012).
[31] N. Takemoto and A. Becker, Phys. Rev. Lett. **105**, 203004 (2010).
[32] N. Takemoto and A. Becker, Phys. Rev. A **84**, 023401 (2011).
[33] T. Zuo and A. D. Bandrauk, Phys. Rev. A **52**, R2511 (1995).
[34] M. Spanner, O. Smirnova, P. B. Corkum, and M. Y. Ivanov, J. Phys. B **37**, L243 (2004).
[35] G. Lagmago Kamta and A. D. Bandrauk, Phys. Rev. A **75**, 041401 (2007).
[36] J. Fernández and L. B. Madsen, Phys. Rev. A **79**, 063406 (2009).
[37] K.-J. Yuan and A. D. Bandrauk, Phys. Rev. A **83**, 063422 (2011).
[38] X. Ren, X. Zhang, Y. Xu, H. Ma, and J. Yang, J. Opt. Soc. Am. B **29**, 2124 (2012).
[39] N. B. Delone and V. P. Krainov, J. Opt. Soc. Am. B **8**, 1207 (1991).
[40] L. Meng, C. O. Reinhold, and R. E. Olson, Phys. Rev. A **40**, 3637 (1989).
[41] A. Emmanouilidou and A. Staudte, Phys. Rev. A **80**, 053415 (2009).
[42] T. K. Kjeldsen, L. B. Madsen, and J. P. Hansen, Phys. Rev. A **74**, 035402 (2006).
[43] C. Huang, Z. Li, Y. Zhou, Q. Tang, Q. Liao, and P. Lu, Opt. Express **20**, 11700 (2012).